

Toward Speed-of-Sound Anisotropy Quantification in Muscle With Pulse-Echo Ultrasound

Naiara Korta Martiartu^{ID}, Saulé Simuté, Michael Jaeger, Thomas Frauenfelder, and Marga B. Rominger^{ID}

Abstract—The velocity of ultrasound longitudinal waves (speed of sound) is emerging as a valuable biomarker for a wide range of diseases, including musculoskeletal disorders. Muscles are fiber-rich tissues that exhibit anisotropic behavior, meaning that velocities vary with the wave-propagation direction. Therefore, quantifying anisotropy is essential to improve velocity estimates while providing a new metric related to muscle composition and architecture. For the first time, this work presents a method to estimate speed-of-sound anisotropy in transversely isotropic tissues using pulse-echo ultrasound. We assume elliptical anisotropy and consider an experimental setup with a flat reflector parallel to the linear probe, with the muscle in between. This setup allows us to measure first-arrival reflection traveltimes using multistatic operation. Unknown muscle parameters are the orientation angle of the anisotropy symmetry axis and the velocities along and across this axis. We derive analytical expressions for the nonlinear relationship between traveltimes and anisotropy parameters, including reflector inclinations. These equations are exact for homogeneous media and are useful to estimate the effective average anisotropy in muscles. To analyze the structure of this forward problem, we formulate the inversion statistically using the Bayesian framework. We demonstrate that anisotropy parameters can be uniquely constrained by combining traveltimes from different reflector inclinations. Numerical results from wide-ranging acquisition and anisotropy properties show that uncertainties in velocity estimates are substantially lower than expected velocity differences in the muscle. Thus, our approach could provide meaningful muscle anisotropy estimates in future clinical applications.

Index Terms—Anisotropy, Bayesian inference, longitudinal waves, muscle, speed of sound, transverse isotropy, ultrasound, uncertainty quantification.

Manuscript received 9 May 2022; accepted 2 July 2022. This work was supported by the Swiss National Supercomputing Centre (CSCS) under Project sm59 and Project s1040. (Corresponding author: Naiara Korta Martiartu.)

Naiara Korta Martiartu was with the Zurich Ultrasound Research and Translation (ZURT) Group, Institute of Diagnostic and Interventional Radiology, University Hospital Zürich, CH-8091 Zürich, Switzerland. She is now with the Institute of Applied Physics, University of Bern, CH-3012 Bern, Switzerland (e-mail: naiara.korta@unibe.ch).

Saulé Simuté was with the Department of Earth Sciences, ETH Zürich, CH-8092 Zürich, Switzerland. She is now with the Swiss Re Institute, Swiss Re, CH-8002 Zürich, Switzerland.

Michael Jaeger is with the Institute of Applied Physics, University of Bern, CH-3012 Bern, Switzerland.

Thomas Frauenfelder and Marga B. Rominger are with the Zurich Ultrasound Research and Translation (ZURT) Group, Institute of Diagnostic and Interventional Radiology, University Hospital Zürich, CH-8091 Zürich, Switzerland.

This article has supplementary downloadable material available at <https://doi.org/10.1109/TUFFC.2022.3189184>, provided by the authors.

Digital Object Identifier 10.1109/TUFFC.2022.3189184

I. INTRODUCTION

SPEED-OF-SOUND estimation in tissue using ultrasound has attracted considerable attention in recent years [1]–[7]. Speed of sound refers to the propagation velocity of longitudinal waves, which are typically used for image formation in ultrasound systems. This property contains clinically relevant information about tissue composition and shows great promise as a biomarker for a wide range of diseases. Clinical applications involving longitudinal-wave velocities include, for instance, breast cancer screening [1], [8], [9], hepatic steatosis assessment [10], [11], and diagnosis of musculoskeletal disorders [12], [13].

Unlike breast and liver tissue, muscles exhibit anisotropic mechanical properties due to their fibrous structure. Velocities vary with the ultrasound wave-propagation direction, showing higher values along fiber direction than across fibers. Empirical studies in *ex vivo* human and animal tissues have reported velocity differences of up to 24 m/s [14]–[18]. Hence, failure to properly account for anisotropy can result in unreliable velocity estimates. Quantifying anisotropy is clinically interesting mainly for two reasons. On the one hand, it can provide improved velocity estimates, which are informative about muscle composition [13]. On the other hand, this property is directly related to the muscle fiber distribution, encoding also information about muscle architecture.

Anisotropy estimation can be particularly relevant for monitoring sarcopenia cost-efficiently. This is an age-related musculoskeletal disorder characterized by the progressive loss of both muscle mass and function. Speed of sound is strongly correlated with reference standards for quantifying muscle mass loss [13] and have proven promising for differentiating young and older populations [12]. However, the loss in muscle mass is not correlated with the loss in muscle function [19], and both are required to assess this pathology accurately [20]. Current standards to measure muscle function, which is related to the muscle fiber arrangement [21], are based on questionnaires or tests [20]; thus, they do not include any quantitative imaging tool. In this context, estimating speed-of-sound anisotropy with ultrasound could bring significant benefits for assessing sarcopenia.

Methods to characterize the anisotropy of (quasi-) longitudinal waves are relatively unexplored in the literature. Studies addressing this topic have only focused on *in vitro* measurements, where experimental setups are not appropriate for clinical examinations [14]–[18]. Characterization of anisotropy in shear waves, on the contrary, is an active research

field. Lee *et al.* [22] developed an approach termed elastic tensor imaging (ETI) to map myocardial fiber directions based on shear-wave anisotropy. ETI uses either linear-probe rotations or 2-D matrix-array probes [23] to measure shear-wave velocities at different propagation directions. From here, fiber orientation angles can be extracted by assuming the medium as transversely isotropic. Measurements in animal myocardial samples have demonstrated strong correlations of ETI with histological data [22] and diffusion tensor magnetic resonance imaging [24]. A similar approach using 2-D matrix probes was also suggested by Wang *et al.* [25], who generalized the method to cases in which the shear-wave excitation push is not perpendicular to fibers. Shear-wave velocity measurements, however, are prone to artifacts caused by tissue inhomogeneities. To circumvent this, Hossain *et al.* [26] proposed measuring tissue peak displacements at locations of the shear-wave excitation source. Variations of this quantity as a function of the probe orientation were seen to correlate with anisotropy in shear moduli [26]. This approach showed promising results, for example, for monitoring the status of renal transplant in humans [27].

Shear and longitudinal waves interrogate fundamentally different but complementary mechanical tissue properties [28]. Due to the acquisition setup of ultrasound systems, they typically propagate in approximately perpendicular directions; thus, we cannot directly extrapolate to longitudinal waves the techniques developed for quantifying shear-wave anisotropy. This work aims to present a method capable of quantifying speed-of-sound anisotropy in muscle using pulse-echo ultrasound. We consider a setup with a flat reflector located opposite the ultrasound probe, allowing us to measure first-arrival reflection traveltimes [4]. In Section II, we derive the analytical expression of the relationship between these traveltimes and muscle anisotropy. Their sensitivity to different anisotropy parameters is discussed in Section III. Section IV briefly introduces the Bayesian inversion approach used in this study. We then analyze the nature of the proposed problem with various numerical examples in Section V. Finally, Section VI summarizes key aspects of the method and carefully discusses its clinical relevance and potential improvements.

II. TRAVELTIME MODELING IN ANISOTROPIC MEDIA

The alignment of fibers in muscles causes anisotropy in mechanical muscle properties. Commonly, muscle tissue is described as a transversely isotropic medium with the symmetry axis along the fiber direction [25], [26], [29], [30]. Such a medium is characterized by five independent elastic parameters, describing, for instance, the longitudinal- and shear-wave velocities along and across the symmetry axis. In soft tissue, however, shear-wave velocities are negligible in comparison to longitudinal-wave velocities [31]. Therefore, it is possible to describe muscle properties using only three independent parameters. In this study, we assume elliptical anisotropy, which is a special case of transverse isotropy. The validity of this assumption is discussed in Appendix A. The three independent parameters are then the orientation angle φ of the anisotropy symmetry axis and the velocities along

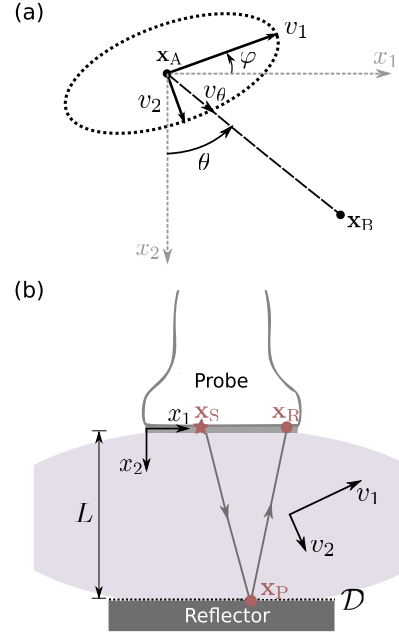


Fig. 1. Schematic representation of the anisotropic medium and experimental setup considered in this study. (a) Wavefronts in elliptically anisotropic media are ellipsoidal. Parameters v_1 and v_2 represent velocities along and across muscle fibers, and φ describes the orientation of fibers with respect to the coordinate system. In an arbitrary propagation direction θ connecting \mathbf{x}_A and \mathbf{x}_B , waves propagate with velocity $v_\theta = v(\theta)$. (b) Our experimental setup includes a flat reflector located opposite the probe, with tissue in between. The probe-reflector distance L is assumed to be controlled by a positioning frame and a digital sensor. We measure first-arrival reflection traveltimes of ultrasound signals emitted from \mathbf{x}_S and received at \mathbf{x}_R , with $\mathbf{x}_P \in D$ indicating the reflection point.

(v_1) and across (v_2) this axis. In such a medium, the group (ray) velocity $v(\theta)$ in an arbitrary propagation direction θ satisfies [32], [33]

$$\frac{v^2(\theta)}{v_1^2} \sin^2(\theta - \varphi) + \frac{v^2(\theta)}{v_2^2} \cos^2(\theta - \varphi) = 1 \quad (1)$$

where the angles θ and φ are illustrated in Fig. 1(a).

Traveltimes of different arrivals are affected by the direction-dependent velocity $v(\theta)$, and we can use them to retrieve anisotropy parameters $\mathbf{m} = (v_1, v_2, \varphi)$. For simplicity, we consider the muscle as a 2-D homogeneous medium. Using (1) and trigonometric identities, the traveltime t_{AB} between positions \mathbf{x}_A and \mathbf{x}_B is given by

$$t_{AB}^2 = \frac{1}{v_1^2} [(x_{1,B} - x_{1,A}) \cos \varphi - (x_{2,B} - x_{2,A}) \sin \varphi]^2 + \frac{1}{v_2^2} [(x_{1,B} - x_{1,A}) \sin \varphi + (x_{2,B} - x_{2,A}) \cos \varphi]^2. \quad (2)$$

The reader is referred to the Supplementary Material for the detailed derivation of equations in this section. From (2), we observe that t_{AB} is nonlinearly related to anisotropic parameters \mathbf{m} . When the orientation of the symmetry axis is known, we obtain a linear relationship between squared traveltimes t^2 and squared slownesses $1/v_1^2$ and $1/v_2^2$.

A. Reflector-Based Experimental Setup

This study considers an experimental setup that includes a reflector located opposite the linear ultrasound probe [see Fig. 1(b)], with the probe-reflector distance L controlled by a positioning frame and a distance sensor [4]. This setup has already been applied in various clinical studies for the assessment of breast [34], [35] and muscle tissue [12], [13], [31], [36]. The reflector allows us to measure first-arrival reflection traveltimes t_{SR} of waves propagating from a source at \mathbf{x}_S to a receiver at \mathbf{x}_R . They can be expressed using Fermat's principle as

$$\min_{\mathbf{x}_P \in \mathcal{D}} t_{SR}(\mathbf{x}_P), \quad \text{where } t_{SR}(\mathbf{x}_P) = t_{SP}(\mathbf{x}_P) + t_{PR}(\mathbf{x}_P) \quad (3)$$

where \mathcal{D} refers to the set of points \mathbf{x}_P at the reflector-tissue interface [see Fig. 1(b)], and traveltimes of each path are computed using (2).

Unlike in isotropic media, the reflection point \mathbf{x}_P^{\min} for the minimum traveltime does not necessarily lie on the midpoint between \mathbf{x}_S and \mathbf{x}_R in anisotropic media. It is possible to show that the location of the reflection point generally satisfies $\mathbf{x}_P^{\min} = ((x_{1,S} + x_{1,R})/2 + \delta, L)$, where δ is a constant value. That is, \mathbf{x}_P^{\min} is shifted from the source-receiver midpoint position by the same constant δ for every source-receiver combination. To find the value of δ , we consider, for simplicity, the zero-offset case in which $\mathbf{x}_S = \mathbf{x}_R$, and we solve (3) using

$$\left. \frac{dt_{SR}}{dx_{1,P}} \right|_{\mathbf{x}_P = \mathbf{x}_P^{\min}} = 2 \left. \frac{dt_{SP}}{d\delta} \right|_{\mathbf{x}_P = \mathbf{x}_P^{\min}} = 0. \quad (4)$$

The reflection point is then

$$\mathbf{x}_P^{\min} = \left(\frac{x_{1,S} + x_{1,R}}{2} + \frac{L \sin 2\varphi (v_2^2 - v_1^2)}{2(v_1^2 \sin^2 \varphi + v_2^2 \cos^2 \varphi)}, L \right). \quad (5)$$

This point is located at the source-receiver midpoint only when the medium is isotropic ($v_1 = v_2$) or the anisotropy symmetry axis is aligned with our coordinate system ($\varphi = 0^\circ$). For muscle tissue, we expect $v_1 > v_2$ for $\varphi \in [-\pi/4, \pi/4]$, i.e., waves propagating faster along than across fiber direction [14]. Therefore, δ can be either positive or negative depending on the sign of φ .

Upon inserting (5) in (2) and (3), we can observe that the path with the minimum traveltime satisfies $t_{SP}(\mathbf{x}_P^{\min}) = t_{PR}(\mathbf{x}_P^{\min})$. Therefore, *the fastest ray path is the path with equal traveltime along each segment*. This also means that the mirror image of the receiver, namely a virtual equivalent receiver $\tilde{\mathbf{R}}$ below the reflector satisfying $t_{S\tilde{R}} = t_{SR}$, is located at $\mathbf{x}_{\tilde{R}} = 2(\mathbf{x}_P^{\min} - \mathbf{x}_S) + \mathbf{x}_S = 2\mathbf{x}_P^{\min} - \mathbf{x}_S$. The first-arrival reflection traveltime between \mathbf{x}_S and \mathbf{x}_R is then

$$t_{SR}^2(\mathbf{x}_P^{\min}) = \frac{d^2}{v^2(\theta = \pi/2)} + \frac{4L^2 v^2(\theta = \pi/2)}{v_1^2 v_2^2} \quad (6)$$

with $v^2(\theta = \pi/2)$ given by (1) and $d = x_{1,R} - x_{1,S}$ being the source-receiver offset. This equation establishes the relationship between observations t_{SR} and unknown muscle properties $\mathbf{m} = (v_1, v_2, \varphi)$. Thus, the forward problem considered in this study is nonlinear. When the anisotropy symmetry axis

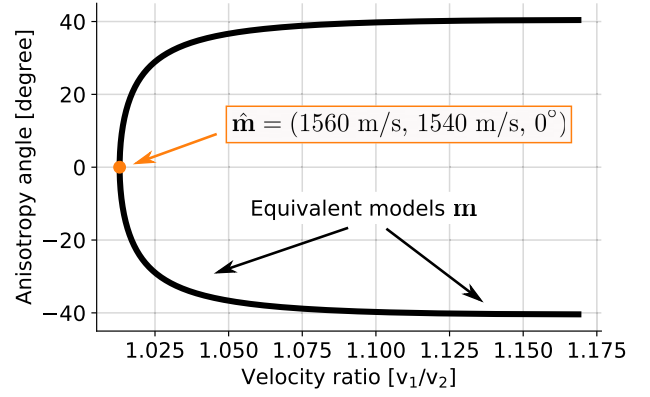


Fig. 2. Muscle models satisfying the conditions (8) and, thus, providing equal traveltimes. For this example, we take the reference model $\hat{\mathbf{m}} = (1560 \text{ m/s}, 1540 \text{ m/s}, 0^\circ)$ and represent equivalent models \mathbf{m} for $\varphi \in [-45^\circ, 45^\circ]$. Because muscle models are defined by three parameters, we represent the anisotropy angle φ versus the velocity ratio v_1/v_2 for visualization. We only show models with velocities in the range of [1300, 1800] m/s.

is aligned with the coordinate system ($\varphi = 0^\circ$), (6) reduces to

$$t_{SR}^2(\mathbf{x}_P^{\min}) = \frac{d^2}{v_1^2} + \frac{4L^2}{v_2^2} \quad (7)$$

and, as previously observed, t_{SR}^2 becomes linearly related to squared slownesses $1/v_1^2$ and $1/v_2^2$. It is important to note that (5) and (6) are exact for any homogeneous media with elliptical anisotropy.

B. Nonuniqueness

In this section, we demonstrate that traveltimes satisfying (6) are not sufficient to constrain muscle properties uniquely. For notational brevity, we omit the dependence on \mathbf{x}_P^{\min} from traveltimes.

Let us assume that we measure traveltimes $t_{SR}^2(\hat{\mathbf{m}})$ in the medium $\hat{\mathbf{m}}$. If $t_{SR}^2(\hat{\mathbf{m}})$ is uniquely defined by $\hat{\mathbf{m}}$, then any other \mathbf{m} giving the same traveltimes $t_{SR}^2(\hat{\mathbf{m}}) = t_{SR}^2(\mathbf{m})$ must satisfy $\hat{\mathbf{m}} = \mathbf{m}$. For simplicity, we take $\hat{\mathbf{m}} = (\hat{v}_1, \hat{v}_2, \hat{\varphi} = 0^\circ)$ and $\mathbf{m} = (v_1, v_2, \varphi)$ and consider a single source-receiver pair. Equating (6) and (7), we see that both muscle parameters give the same traveltimes when

$$\hat{v}_1 \hat{v}_2 = v_1 v_2 \quad (8a)$$

$$v_1^2 \sin^2 \varphi + v_2^2 \cos^2 \varphi = \hat{v}_2^2. \quad (8b)$$

These conditions can be satisfied for $\hat{\mathbf{m}} \neq \mathbf{m}$ even when we exclude the intrinsic periodicity of φ [i.e., $\mathbf{m}(\varphi) = \mathbf{m}(\varphi + \pi)$] and the obvious symmetry of the elliptical anisotropy ($v_1 \rightarrow v_2$ when $\varphi \rightarrow \varphi + \pi/2$). Thus, traveltimes defined in (6) cannot uniquely constrain muscle anisotropy. It is noted that multiple sources cannot resolve this nonuniqueness because the conditions (8) do not depend on source and receiver locations. As an example, Fig. 2 shows all equivalent muscle models (in terms of traveltimes) to the reference model $\hat{\mathbf{m}} = (1560 \text{ m/s}, 1540 \text{ m/s}, 0^\circ)$. We observe that specially the parameter φ is unconstrained by the forward problem in (6). Hence, we require additional types of observations.

C. Reflector Inclination: Sources of Uncertainties as New Constraints

The simplest way to constrain the anisotropy angle is by combining data acquired from multiple muscle sides. This is equivalent to rotating the tissue with respect to the probe. For *in vivo* studies, however, we can only access the muscle from a single side of the anisotropy plane. To circumvent this limitation, we suggest taking advantage of the reflector inclination, which is unavoidable in practice and regarded as a source of uncertainties [37]. A tilted reflector will generate ray paths with orientations that are different from our previous setup. Therefore, we suggest combining data from multiple inclination angles to constrain muscle anisotropy. In the following, we assume that the inclination angle is controlled using, for instance, B-mode images, and we derive the corresponding forward problem.

Let us denote α the reflector inclination angle with respect to the x_1 -axis, shown in Fig. 3(a). We can use our previous equations by rotating the whole setup to align the reflector with the x_1 -axis. In this situation, the anisotropy angle becomes $\varphi \rightarrow \varphi + \alpha$, the probe is inclined by α with respect to the x_1 -axis, and the vertical probe-reflector distance becomes $L \rightarrow L \cos \alpha$ [see Fig. 3(b)]. Using geometrical identities and the previous result in (5), the reflection point $\mathbf{x}_P^{\min} = (x_{1,P}^{\min}, L \cos \alpha)$ in the rotated system becomes

$$x_{1,P}^{\min} = d_S \cos \alpha + \frac{L'(d \cos \alpha + 2\delta')}{2L' + d \sin \alpha} \quad (9)$$

with

$$\delta' = \frac{(L' + d \sin \alpha) \sin(2(\varphi + \alpha))(v_2^2 - v_1^2)}{2(v_1^2 \sin^2(\varphi + \alpha) + v_2^2 \cos^2(\varphi + \alpha))} \quad (10)$$

and

$$L' = L \cos \alpha + d_S \sin \alpha \quad (11)$$

where d_S denotes the distance between the origin of the coordinate system (first element of the probe) and \mathbf{x}_S , and d is, as previously defined, the distance between \mathbf{x}_S and \mathbf{x}_R .

We replace \mathbf{x}_P^{\min} in (2) and (3) to find the total traveltime

$$t_{SR}^2 = \frac{d^2}{v^2(\pi/2)} + \frac{4L'(L' + d \sin \alpha)}{v_1^2 \sin^2(\varphi + \alpha) + v_2^2 \cos^2(\varphi + \alpha)}. \quad (12)$$

This equation is the generalization of (6), which we obtain when $\alpha = 0$.

D. Constraining Anisotropy Parameters

In the following, we demonstrate that we can constrain the muscle anisotropy by combining traveltimes from different reflector inclinations. Since (12) is the generalization of (6), we expect that traveltimes measured from a single reflector inclination show the same nonunique behavior as in Section II-B. Thus, we will first derive the equivalent models, in terms of traveltimes, to a reference model $\hat{\mathbf{m}}$ for an experiment with $\alpha \neq 0^\circ$. We then compare these models with those obtained for $\alpha = 0^\circ$ [see (8)]. If combining traveltimes from these two experiments constrains muscle anisotropy, then

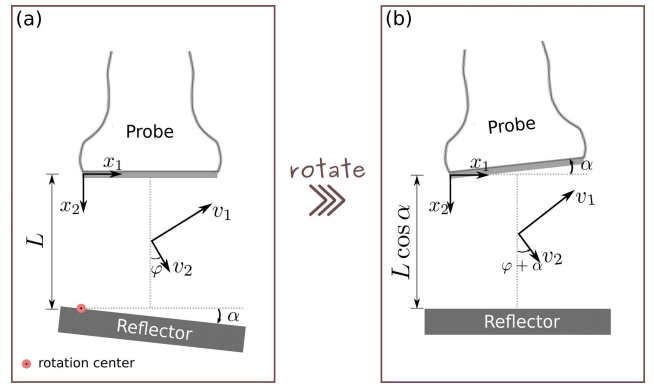


Fig. 3. Schematic illustration showing two equivalent experimental setups. (a) Our original setup considers the reflector inclined by α with respect to the x_1 -axis. The vertical distance, i.e., the distance in x_2 -direction, between the first transducer element (origin of the coordinate system) and the reflector is L . The orientation of the anisotropy symmetry axis is φ . (b) We rotate the whole system by α , with the rotation center indicated in (a), to find an equivalent setup with no reflector inclination. Now, the probe is inclined with respect to the x_1 -axis, the anisotropy angle is $\varphi + \alpha$, and the vertical probe-reflector distance becomes $L \cos \alpha$.

the equivalent models for $\alpha \neq 0^\circ$ and $\alpha = 0^\circ$ should overlap in a single point equal to $\hat{\mathbf{m}}$.

Assume we measure the traveltimes $t_{SR}^2(\hat{\mathbf{m}}; \alpha)$ from muscle properties $\hat{\mathbf{m}}$ using the reflector inclination α . Following the analysis in Section II-B, we can observe that different muscle properties $\mathbf{m} \neq \hat{\mathbf{m}}$ can provide identical traveltimes $t_{SR}^2(\mathbf{m}; \alpha) = t_{SR}^2(\hat{\mathbf{m}}; \alpha)$ using the same experimental setup. Again, we take $\hat{\mathbf{m}} = (\hat{v}_1, \hat{v}_2, \hat{\varphi} = 0^\circ)$ and $\mathbf{m} = (v_1, v_2, \varphi)$ and consider a single source–receiver pair for simplicity. Using (12), we find that equivalent muscle parameters satisfy the conditions

$$\hat{d}_1^2 = \frac{v_1^2 v_2^2}{v_1^2 \sin^2 \varphi + v_2^2 \cos^2 \varphi} \quad (13a)$$

$$\hat{d}_1^2 \sin^2 \alpha + \hat{d}_2^2 \cos^2 \alpha = v_1^2 \sin^2 \varphi_\alpha + v_2^2 \cos^2 \varphi_\alpha \quad (13b)$$

where $\varphi_\alpha = \varphi + \alpha$. These conditions reduce to (8) for $\alpha = 0^\circ$.

To understand the meaning of (13), we take the reference model $\hat{\mathbf{m}} = (1560 \text{ m/s}, 1540 \text{ m/s}, 0^\circ)$, same as in Section II-B, and represent models satisfying (13) for different values of α , shown in Fig. 4. We observe that our reference model $\hat{\mathbf{m}}$ is the only model in common for different reflector inclinations. This demonstrates that combining traveltimes from different α can uniquely constrain muscle anisotropy. We also observe that the sets of equivalent models differ more for larger differences in α . Consequently, in the presence of measurement noise, we expect to constrain the anisotropy more accurately by combining traveltimes from setups with larger inclination differences. In the extreme case where we combine $\alpha = 0^\circ$ and $\alpha = 90^\circ$, observed traveltimes will correspond to perpendicular ray paths that can measure muscle anisotropy directly. However, a large reflector inclination will deform muscle tissue considerably, changing its anisotropic properties. We should therefore avoid large inclinations in practice to minimize the realignment of fibers and obtain consistent measurements.

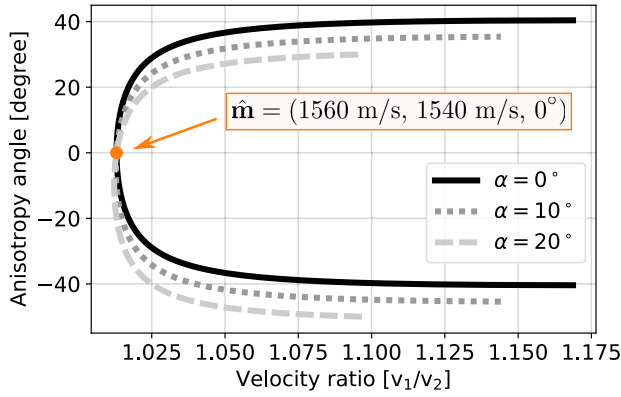


Fig. 4. Muscle models satisfying the conditions (13a) and providing same traveltimes for reflector inclination angles $\alpha = 0^\circ$, 10° , and 20° . For all α , the reference model is $\hat{\mathbf{m}} = (1560 \text{ m/s}, 1540 \text{ m/s}, 0^\circ)$, and we represent its equivalent models for $\varphi \in [-45^\circ, 45^\circ]$ and $v_1, v_2 \in [1300, 1800] \text{ m/s}$. The Supplementary Material includes the same figure with respect to v_1 and v_2 for clarity.

E. Validation With Numerical Simulations

The derivations presented previously are sufficient to demonstrate that (12) is exact for homogeneous media with elliptical anisotropy. In this section, we confirm this with simulations that solve the wave equation numerically. We use the spectral-element solver Salvus [38] to model the wave propagation in muscle using the 2-D time-domain elastic wave equation with shear modulus equal to zero, i.e.,

$$\rho \partial_t^2 u(\mathbf{x}, t) - \nabla \cdot (\mathbf{D} \nabla u(\mathbf{x}, t)) = f(\mathbf{x}_S, t). \quad (14)$$

Here, f is the external source generated from \mathbf{x}_S , u is the scalar displacement potential, ρ is the muscle density, and \mathbf{D} is a second-order symmetric positive tensor describing the direction-dependent velocities v . If the anisotropy is aligned with the coordinate system, \mathbf{D} is a diagonal matrix with elements $D_{11} = \rho v_1^2$ and $D_{22} = \rho v_2^2$. For tilted anisotropy, we apply the rotation matrix to derive the elements of \mathbf{D} .

To simulate the reflector-based experimental setup, we use a medium with two homogeneous layers representing the muscle and reflector. The muscle layer is elliptically anisotropic with density 1000 kg/m^3 . The reflector is isotropic with speed of sound 2670 m/s and density 1180 kg/m^3 , simulating a polymethylmethacrylate material [4]. The probe consists of 128 transducer elements with 0.3-mm pitch. We use the first element to transmit a pulse of 2.5-MHz center frequency while all elements act as receivers. It is noted that our frequencies are lower than those typically used in linear probes to keep simulations computationally affordable.

We illustrate the accuracy of our forward model in (12) using the muscle model $\mathbf{m} = (1560 \text{ m/s}, 1540 \text{ m/s}, 5^\circ)$, a probe-reflector distance of $L = 8 \text{ cm}$, and reflector inclination angles $\alpha = 0^\circ$ and $\alpha = 5^\circ$. First-arrival reflection traveltimes are computed by cross-correlating recorded signals with a simulated calibration dataset in water (1515 m/s) using the same experimental setup. Fig. 5 compares traveltimes measured from wave propagation simulations with those analytically modeled using (12). As expected, both examples

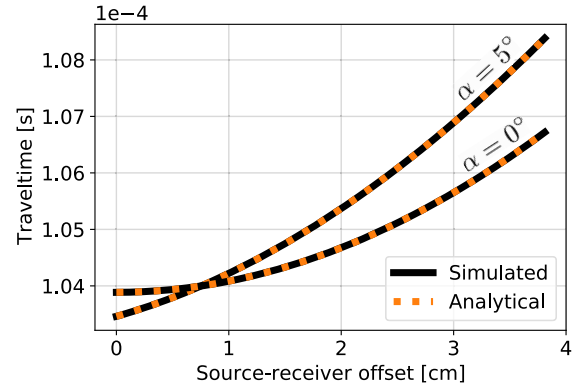


Fig. 5. Comparison of *simulated* traveltimes from numerical wave propagation simulations with those *analytically* modeled using (12). The source is located at the first transducer element, and traveltimes are represented with respect to the source–receiver offset. We used the muscle model $\mathbf{m} = (1560 \text{ m/s}, 1540 \text{ m/s}, 5^\circ)$, the probe-reflector distance $L = 8 \text{ cm}$, and reflector inclination angles $\alpha = 0^\circ$ and $\alpha = 5^\circ$. Root mean square errors are $8.10 \cdot 10^{-10} \text{ s}$ and $8.34 \cdot 10^{-10} \text{ s}$ for $\alpha = 0^\circ$ and $\alpha = 5^\circ$, respectively.

show negligible differences between simulated and analytical traveltimes demonstrating that (12) is exact.

III. TRAVELTIME SENSITIVITIES TO TISSUE ANISOTROPY

Partial derivatives of traveltimes with respect to different anisotropy parameters contain valuable information on the expected reconstruction accuracy. They reveal how sensitive traveltimes are to changes in anisotropic parameters; thus, we can analyze them to understand how well model parameters can be constrained from specific traveltime observations.

So far, we have assumed that we can control the reflector inclination angle, for instance, from B-mode images. However, due to unknown tissue properties, this estimation will contain uncertainties, and reconstruction algorithms should consider α as another parameter to retrieve within \mathbf{m} . Hence, we also analyze the traveltime sensitivity with respect to α .

Since our forward problem is nonlinear, the sensitivities depend on model parameters. Still, we can make interesting observations by analyzing their values for the same model and acquisition parameters used in Fig. 5 [see Fig. 6]. In this case, traveltime sensitivities to v_1 are approximately one order of magnitude lower than the sensitivities to v_2 . This is caused by the limited aperture of the ultrasound probe, as suggested by the magnitude increase with the source–receiver offset. Increasing the reflector inclination angle increases the components of ray paths along x_1 -direction, and traveltimes become more sensitive to v_1 . Similarly, the sensitivities to v_2 weaken with increasing the source–receiver offset and reflector inclination angle. Accordingly, we expect higher uncertainties in the estimation of v_1 than v_2 for $\varphi < \pi/4$.

Traveltime sensitivities to φ change substantially with α compared to the changes with respect to the source–receiver offset, suggesting a strong nonlinear relationship between traveltimes and φ . This is not surprising, as traveltimes depend on φ through trigonometric functions. The magnitude of these sensitivities in Fig. 6 is therefore difficult to interpret. Finally,

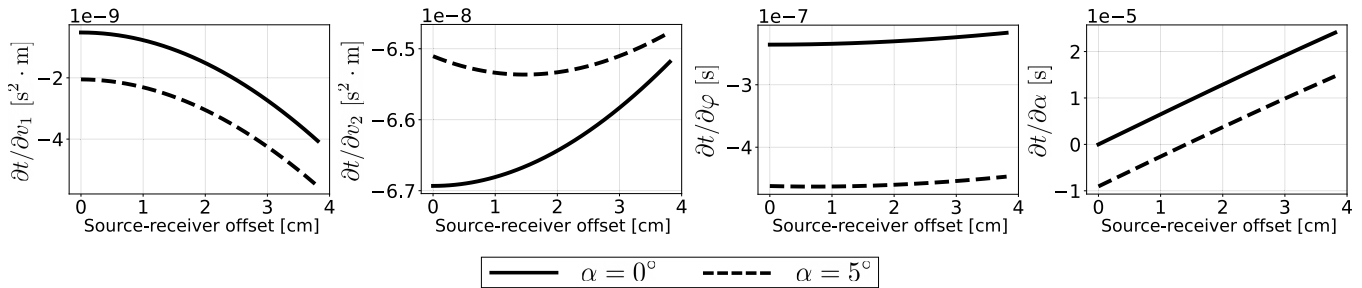


Fig. 6. Sensitivities of traveltimes to velocities along (v_1) and across (v_2) the anisotropy symmetry axis, the orientation of this axis (φ), and the reflector inclination angle (α), respectively. The sensitivities are shown as a function of the source-receiver offset to illustrate its variability. We consider the same anisotropy and acquisition parameters as in Fig. 5.

we observe that traveltimes are highly sensitive to α , with values approximately four orders of magnitude larger than those for v_1 . It means that traveltimes are very informative about the reflector inclination angle, which we expect to retrieve with high accuracy.

IV. STATISTICAL INVERSE PROBLEM

Estimating muscle anisotropy from traveltime observations involves solving a nonlinear inverse problem. In principle, we can formulate this as a gradient-based optimization problem to search for the model \mathbf{m} that minimizes the misfit between observed traveltimes \mathbf{d}_{obs} and predicted traveltimes \mathbf{d} [39]. Such deterministic approaches, however, cannot guarantee that the solution corresponds to the global minimum of the nonlinear function we try to minimize. They are also incapable of accurately estimating uncertainties in the solution caused by measurement noise, limited data coverage, and inaccurate forward modeling [40]. In this study, our goal is to analyze the feasibility of estimating the speed-of-sound anisotropy from traveltime observations. For this analysis, quantifying uncertainties is crucial; thus, we address the inversion statistically using the Bayesian framework. The solution is a posterior probability density function (pdf) $\pi_{\text{post}}(\mathbf{m}|\mathbf{d}_{\text{obs}})$ that contains the complete statistical description of model parameters [39], [40].

According to Bayes' theorem [41], [42], the posterior pdf satisfies

$$\pi_{\text{post}}(\mathbf{m}|\mathbf{d}_{\text{obs}}) = k \pi_{\text{prior}}(\mathbf{m})\pi_{\text{like}}(\mathbf{d}_{\text{obs}}|\mathbf{m}) \quad (15)$$

where k is an appropriate normalization constant, $\pi_{\text{prior}}(\mathbf{m})$ encodes our prior information on \mathbf{m} , and the data likelihood $\pi_{\text{like}}(\mathbf{d}_{\text{obs}}|\mathbf{m})$ is the conditional probability of having observations \mathbf{d}_{obs} given the model \mathbf{m} . We can express the data likelihood explicitly as

$$\pi_{\text{like}}(\mathbf{d}_{\text{obs}}|\mathbf{m}) \propto \exp\left[-\frac{1}{2}(\mathbf{d} - \mathbf{d}_{\text{obs}})^T \mathbf{\Gamma}_n^{-1}(\mathbf{d} - \mathbf{d}_{\text{obs}})\right] \quad (16)$$

where $\mathbf{d} = \mathbf{F}(\mathbf{m})$ is the forward problem in (12), and $\mathbf{\Gamma}_n$ is the noise covariance matrix describing normally distributed uncertainties in observations. Here, we assume that traveltimes are measured using reflector delineation techniques suggested in the literature [4], [43]. These techniques were developed to measure the traveltimes of waves propagating from single-element emitters, the same observables as in our case. Since

traveltimes vary smoothly between adjacent receivers, delineation approaches incorporate this prior knowledge to remove outliers, minimizing large measurement errors.

In principle, the prior $\pi_{\text{prior}}(\mathbf{m})$ can take any form. We can generally express it in terms of individual model parameters m_i as

$$\pi_{\text{prior}}(\mathbf{m}) = \prod_{i=1}^N \pi_{\text{prior}}(m_i) \quad (17)$$

where N is the number of parameters in \mathbf{m} . In this study, we use either a uniform distribution between a fixed range of values, i.e.,

$$\pi_{\text{prior}}(m_i) = \begin{cases} \frac{1}{m_i^{\text{max}} - m_i^{\text{min}}}, & \text{if } m_i \in [m_i^{\text{min}}, m_i^{\text{max}}] \\ 0, & \text{otherwise} \end{cases} \quad (18)$$

or a Gaussian distribution

$$\pi_{\text{prior}}(m_i) = \frac{1}{\sqrt{2\pi}\sigma_i} \exp\left[-\frac{(m_i - m_i^0)^2}{2\sigma_i^2}\right] \quad (19)$$

with mean m_i^0 and standard deviation σ_i . We consider broad uniform priors for velocities and anisotropy angle. Such priors are relatively uninformative, simulating a scenario with little previous knowledge about the medium. While we could use more sophisticated forms of prior, for instance, including correlations between anisotropic parameters, the uniform prior allows us to understand better the constraints imposed by the traveltime data. When reflector inclination angles are considered part of \mathbf{m} , we use Gaussian priors for these parameters. Here, we assume that approximate values of inclination angles are available from B-mode images.

The posterior allows us to extract useful statistical information about muscle anisotropic parameters. For instance, we can compute the probability of \mathbf{m} satisfying certain conditions \mathcal{M}_1 of clinical interest as $P(\mathbf{m} \in \mathcal{M}_1) = \int_{\mathcal{M}_1} \pi_{\text{post}}(\mathbf{m}|\mathbf{d}_{\text{obs}})\mathbf{d}\mathbf{m}$. This probability can be relevant in clinical decision-making when disease-related thresholds exist for anisotropic parameters. Other statistical quantities such as the expectation or marginal pdfs are also computed via similar integrals.

Unless the forward problem is linear, and the prior and noise are Gaussian, analytical expressions of the posterior are not available [39], [44]. Still, it is possible to approximate the statistical information contained in the posterior using

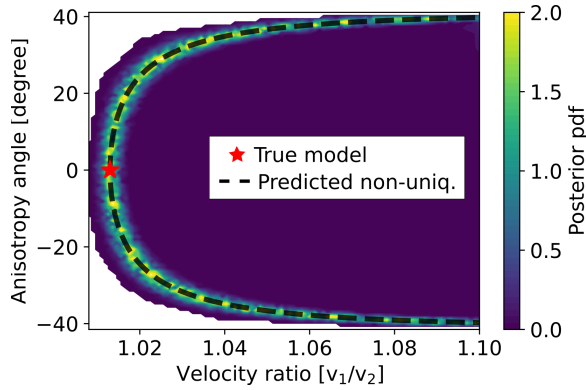


Fig. 7. Posterior pdf related to the unconstrained forward problem in (6). We consider 32 sources equidistantly located and the source-reflector distance $L = 8$ cm. Models with highest pdf correspond to theoretically predicted ones in Fig. 2 (dashed line). They explain equally well the traveltimes computed from the true model (red star).

efficient sampling techniques. In this study, we employ the Metropolis-Hastings Markov chain Monte Carlo (MCMC) algorithm [45]–[47]. The algorithm generates an ensemble of random samples of the posterior with sampling density proportional to $\pi_{\text{post}}(\mathbf{m}|\mathbf{d}_{\text{obs}})$. We can use this ensemble to approximate integrals related to our statistical quantities of interest.

V. NUMERICAL EXAMPLES

In this section, we show numerical examples illustrating the nature of the anisotropy estimation problem. Our objectives are threefold: 1) show the role of the reflector inclination in constraining anisotropy parameters; 2) investigate the robustness of the problem under uncertain inclination angles and a mismatch in probe-reflector distance between measurements; and 3) understand the impact of the experimental setup, anisotropy properties, and measurement noise on solution uncertainties.

All examples shown here consider a uniform prior for velocities and anisotropy angle within the range of [1300 m/s, 1800 m/s] and $[-45^\circ, 45^\circ]$, respectively. As in Section II-E, we use an ultrasound probe with 128 transducer elements and 0.3-mm pitch. We consider every fourth element acting as a source sequentially (a total of 32 sources) while all elements are in receiving mode. Following reported values in [43], where the authors compare annotated first-arrival reflection traveltimes with those estimated from reflector delineation approaches, we assume Gaussian observational errors with a standard deviation of 0.1% of maximum traveltimes. To ensure convergence and correctly interpret the statistical results, we explore the posterior with a relatively large number of random samples, $\mathcal{O}(10^7)$, although fewer samples could suffice for practical purposes.

A. Unconstrained Problem

In this example, we solve the Bayesian anisotropy inference using the forward problem in (6). Our goal is to illustrate how the nonuniqueness of the forward problem is mapped into the posterior. We consider the same example as in Fig. 2, where the true model is $\mathbf{m}_{\text{true}} = (1560 \text{ m/s}, 1540 \text{ m/s}, 0^\circ)$,

and the probe-reflector distance is $L = 8$ cm. Our *artificial* observations of traveltimes are numerically computed from (6) and collected in the vector \mathbf{d}_{obs} , which contains a total of 32×128 traveltimes. Fig. 7 shows the solution of the inverse problem, namely the posterior pdf. Models with maximum posterior probability densities are same as those theoretically predicted in Fig. 2 and explain the observations equally likely. This example demonstrates moreover that including multiple sources does not improve the nonuniqueness of (6), as previously noted. Unless our prior is stronger than a uniform distribution, the posterior will show the exact same nonuniqueness of the forward problem. In this example, however, a stronger prior would dominate the solution. For instance, a Gaussian prior would produce a maximum a posteriori point at the same location of the prior’s maximum, which may not represent the true model. Hence, one should carefully interpret the posterior when the data are not informative enough on model parameters.

B. Constrained Problem

We illustrate here how the problem can be constrained by combining data from multiple reflector inclinations. We consider the same true model and acquisition setup as in the previous example. Now, our artificial observables are $2 \times 32 \times 128$ traveltimes obtained with reflector inclination angles $\alpha = 0^\circ$ and $\alpha = 5^\circ$ using (12). Fig. 8(a) shows the posterior pdf for this case, which has a unique maximum that matches the true model location. Unlike the previous example, now traveltimes are able to constrain a unique set of model parameters. We can quantify uncertainties in the solution using marginal pdfs for each model parameter, shown in Fig. 8(b). Although the problem is nonlinear, the posterior pdf approximates a multivariate Gaussian distribution. We thus express the solution using the mean and standard deviation of the Gaussian fit of the marginals, which is useful to quantify uncertainties. Mean values accurately predict true model parameters with standard deviations less than 1.62 m/s for velocities and 0.61° for the anisotropy angle. As predicted in Section III, we observe that v_1 is less constrained than v_2 due to the limited aperture of the probe.

C. Uncertain Reflector Inclination

In Section III, we observed that traveltimes are highly sensitive to the reflector inclination angle. As a result, if we use inaccurate values of α in the forward problem, we may expect meaningless solutions. This is illustrated in Fig. 9(a), where we consider the same example as before but with errors of 5° in reflector inclination angles. That is, we fix the values of α as 5° and 10° instead of 0° and 5° to invert anisotropy parameters. The marginal pdfs show that reconstructed parameters deviate strongly from the true values. Their mean values provide a model with a negative log-posterior value of $2.74e5$, meaning that there is a substantial mismatch between observed and predicted traveltimes. To circumvent this issue, we suggest extending the Bayesian formulation by including inclination angles as unknown model parameters, i.e., $\mathbf{m} = (v_1, v_2, \varphi, \alpha_1, \alpha_2)$. This also allows

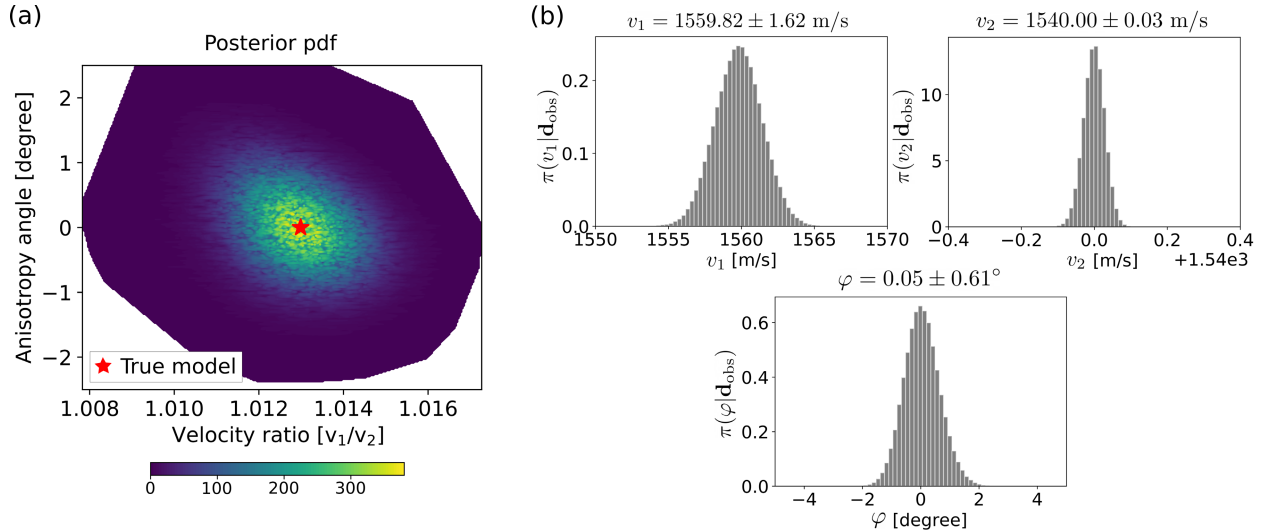


Fig. 8. (a) Posterior pdf when traveltimes from two different reflector inclinations (0° and 5°) are considered. We use the same true model (red star) and acquisition setup as in Fig. 7. Unsamped models by the algorithm are shown as white areas. The posterior has a unique maximum indicating that model parameters are well constrained by the traveltimes. (b) Marginal pdfs for v_1 , v_2 , and φ , respectively. The marginals are histograms obtained with the MCMC algorithm and represent the sampling frequency of the values for each model parameter. The solution for each parameter is given in terms of the mean and standard deviation, shown on top of the histograms. The velocity across fibers (v_2) is better constrained than the velocity parallel to fibers (v_1).

us to incorporate in the prior pdf our rough estimations and uncertainties of α_1 and α_2 . To be consistent with the previous example, we assume Gaussian priors with means at 5° and 10° and a standard deviation of 3° . That is, we shift Gaussian means by 5° from true values, with a standard deviation that excludes the true values from most probable setups. Although derivations provided in Section II-D are not sufficient to demonstrate the solution uniqueness in this case, the marginal pdfs shown in Fig. 9(b) (in gray) have a clear, unique maximum for each parameter. We show in the Supplementary Material that different MCMC realizations converge to the same posterior pdf, suggesting that the solution uniqueness is still given within the model subspace defined by the priors. The model based on mean values of marginal pdfs has a negative log-posterior value of 15.11; thus, it predicts observed traveltimes accurately. This result demonstrates that the anisotropy estimation is robust against uncertainties in reflector inclinations when the extended Bayesian formulation is used. The most sensitive parameters are v_2 and φ , with uncertainties that increase more than two times compared to those in Fig. 8. Furthermore, the posterior provides accurate values for α_1 and α_2 , despite the substantial deviations between their prior means and true values. This indicates that the data likelihood is sufficiently informative about reflector inclination angles, as already observed in Section III. Thus, one should always consider reflector inclination angles as model parameters to retrieve meaningful anisotropy parameters.

D. Probe-Reflector Distance Mismatch

In practice, varying the reflector inclination angle between measurements could alter the probe-reflector distance. To understand how this affects the inversion and particularly the uniqueness of the forward problem, we consider the same example as before, but with traveltimes measured using

$L = 8$ cm for α_1 and $L = 7$ cm for α_2 . The marginal pdfs obtained in this case are shown in pink in Fig. 9(b). Compared to our previous example, the solution is almost unaffected. Again, the mean values correctly represent the true model. However, the anisotropy angle becomes slightly more uncertain, whereas the standard deviation of v_1 is reduced. The reduced probe-reflector distance may explain the latter. In this case, the components of ray paths along v_1 -direction are increased, constraining the parameter better. This result shows that a correct solution is still guaranteed when a mismatch in L exists between different reflector inclinations.

E. Impact of Experimental Setup, Anisotropy Properties, and Data Noise

Previous results suggest that experimental conditions influence the uncertainties of retrieved parameters. Here, we analyze these effects more in detail when the following five aspects are modified separately: the probe-reflector distance L , the true anisotropy angle φ_{true} , the true velocity differences $\Delta v_{\text{true}} = v_{1,\text{true}} - v_{2,\text{true}}$, the reflector inclination angle $\alpha_{2,\text{true}}$ while $\alpha_{1,\text{true}} = 0^\circ$, and the standard deviation of observational errors σ_{noise} . All examples consider the reference model $\mathbf{m}_{\text{true}} = (1560 \text{ m/s}, 1540 \text{ m/s}, 0^\circ, 0^\circ, 5^\circ)$, and distance $L = 8$ cm, same as in previous examples. Fig. 10 shows how the standard deviations of inverted model parameters vary in each case. As observed before, uncertainties in v_1 decrease when ray paths become closer to v_1 -direction, either by decreasing L [see Fig. 10(a)] or by increasing the φ_{true} [see Fig. 10(b)]. The latter also increases uncertainties in v_2 due to the opposite effect of ray paths in this case. As a result, both velocities would be equally constrained when $\varphi_{\text{true}} = 45^\circ$. Interestingly, varying Δv_{true} [see Fig. 10(c)] or α_2 [see Fig. 10(d)] do not affect v_1 and v_2 , but φ becomes

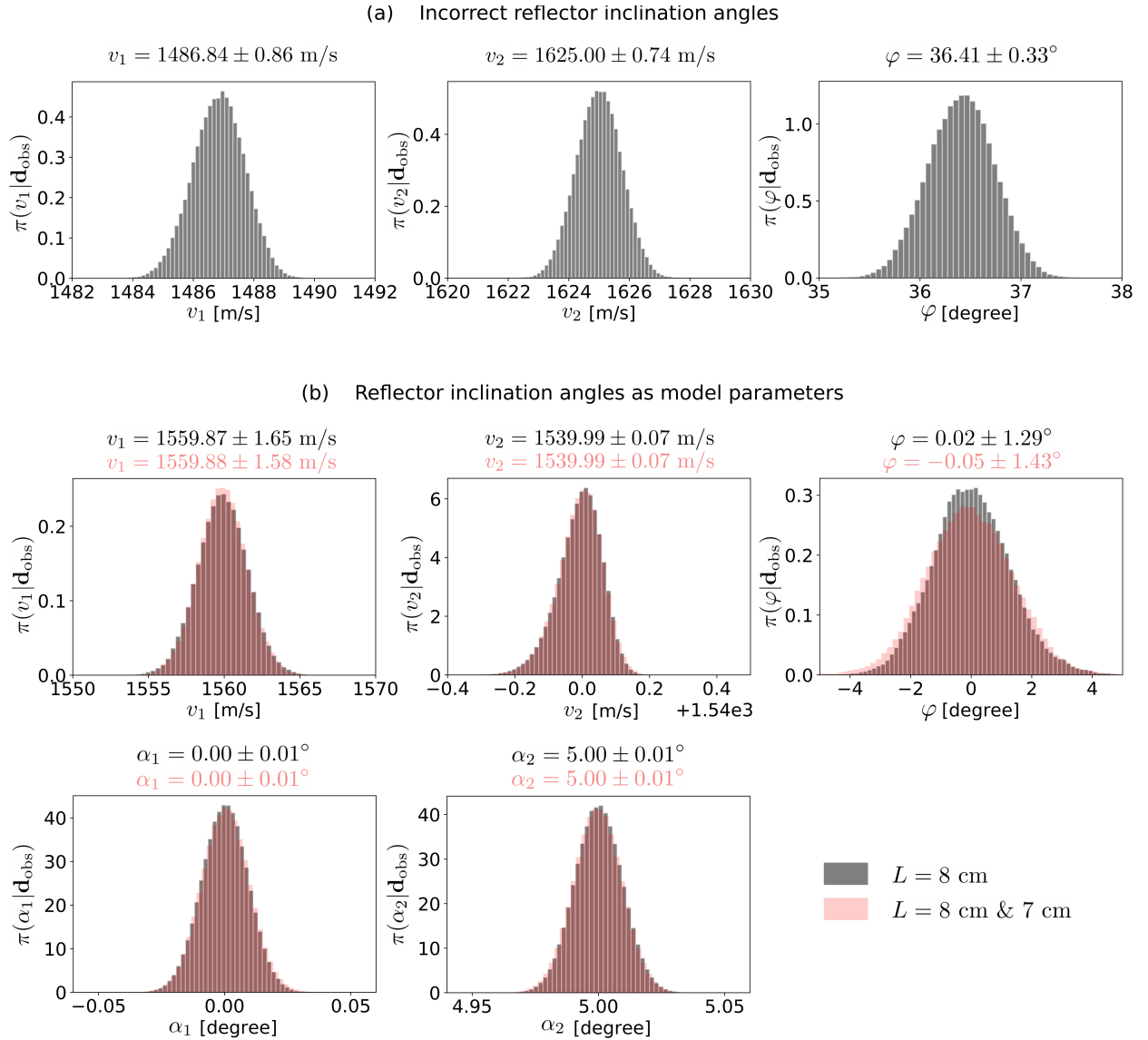


Fig. 9. Marginal pdfs of model parameters. We use the true model $\mathbf{m}_{\text{true}} = (1560 \text{ m/s}, 1540 \text{ m/s}, 0^\circ)$ and reflector inclination angles 0° and 5° to generate artificial observables. (a) Inversion includes an error of 5° in reflector inclinations. As a result, anisotropy parameters with the highest probabilities deviate strongly from true values (negative log-posterior: $2.74\text{e}5$). (b) Inversion considers reflection inclination angles α_1 and α_2 as model parameters to retrieve. Inclination angles have Gaussian priors with their mean shifted 5° from true values and 3° standard deviation. In gray, we show results when probe-reflector distance L is 8 cm, same as in (a). The solution for each parameter is given in terms of the mean and standard deviation, shown on top of histograms. Mean values of marginals accurately predict true anisotropy parameters (negative log-posterior: 15.11). In pink, we show results when we use $L = 8$ cm for α_1 and $L = 7$ cm for α_2 . A mismatch in L between measurements has no significant effects, and the correct solution is still guaranteed.

less constrained when these are small. The effect with Δv_{true} is related to the forward problem in (12), which shows that traveltimes become independent of φ when the medium is isotropic. Therefore, we expect larger uncertainties in φ when approaching isotropic conditions. The effect with α_2 , on the other hand, is related to the nonuniqueness of the forward problem. As analyzed in Fig. 4, model parameters are more difficult to constrain as differences between α_1 and α_2 become smaller. When $\alpha_1 = \alpha_2$, the problem is nonunique, and φ cannot be constrained, explaining the large uncertainties in φ when $\alpha_2 \rightarrow 0$. In all these cases, standard deviations of reflector inclination angles remain constant, suggesting that they are nearly uncorrelated to other model parameters.

In general, we observe that the method is capable of accurately distinguishing velocity differences larger than 4 m/s when observational errors are 0.1% of maximum traveltimes [43]. This is substantially smaller than velocity differences in muscle reported in the literature (>10 m/s) [14]–[17]. Fig. 10(e) shows, however, that parameter uncertainties will increase linearly with σ_{noise} . Still, we could distinguish velocity differences larger than 10 m/s for $\sigma_{\text{noise}} \leq 0.2\%$, which is a considerable increase in noise. Note moreover that uncertainties could be reduced by including more sources in our examples. Therefore, the method presented here has the potential to provide accurate and statistically meaningful muscle anisotropy estimates in future clinical applications.

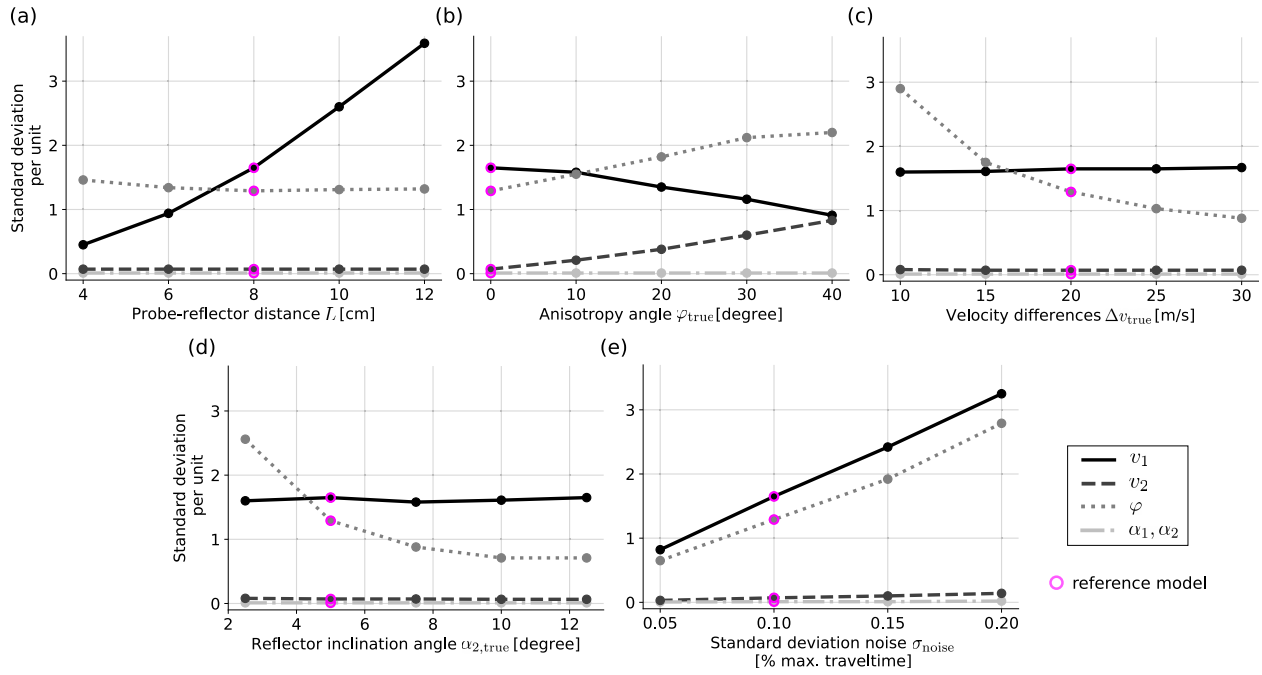


Fig. 10. Standard deviations of model parameters as a function of experimental setup, medium properties, and standard deviation of noise. The reference model and experimental parameters (pink circles) are $\mathbf{m}_{\text{true}} = (1560 \text{ m/s}, 1540 \text{ m/s}, 0^\circ, 0^\circ, 5^\circ)$ and $L = 8 \text{ cm}$, respectively. We modify (a) probe-reflector distance L from 4 to 12 cm, (b) true anisotropy angle φ_{true} from 0° to 40° , (c) true velocity differences $\Delta v_{\text{true}} = v_{1,\text{true}} - v_{2,\text{true}}$ from 10 to 30 m/s, (d) reflector inclination angle α from 2.5° to 12.5° , and (e) standard deviation of traveltime observations from 0.05% to 0.2% of maximum traveltimes. In general, we can distinguish velocity differences larger than 4 m/s when the standard deviation of noise is 0.1%, as reported in [43].

VI. DISCUSSION AND CONCLUSION

This article presents a novel method to estimate the speed-of-sound anisotropy in transversely isotropic tissue. Until now, only shear waves have been used to characterize tissue anisotropy in clinical applications [22], [23], [25], [26], [30], [48], [49]. However, shear and longitudinal waves interrogate fundamentally different mechanical tissue properties [28]. Their propagation velocities differ by three orders of magnitude, resulting in decoupled relationships between the two velocities and elastic moduli [31]. Hence, our work not only complements other studies on the topic but is pivotal to characterize mechanical tissue properties comprehensively.

Due to the lack of previous works on tissue speed-of-sound anisotropy imaging, our work focuses on developing simplified models that provide an essential theoretical basis to understand the nature of the problem. In this respect, we target the average tissue anisotropy by modeling muscles as homogeneous media. Rather than being intrinsic, muscle anisotropy is caused by fine-scale heterogeneities in medium properties (fibers), which we implicitly consider in our formulation. However, local large-scale heterogeneities may also influence the average anisotropy estimates, hindering their interpretation. While being beyond the scope of this article, one could use the effective medium theory to establish the link between heterogeneities and anisotropy [50], [51]. From a clinical interest perspective, this link is key to correlating anisotropy parameters to muscle composition and architecture, which are affected by musculoskeletal disorders. For instance, a change in the number and type of fibers is expected to lead to changes in the average muscle anisotropy. Therefore,

quantifying this property with ultrasound could ultimately provide a cost-efficient, multiparametric biomarker to assess disease-related changes in muscle mass and function.

The method presented here relies on an experimental setup that includes a reflector parallel to the linear probe, with a sensor controlling their distance. This setup can be easily implemented in conventional ultrasound systems and has already been successfully applied in various clinical studies [12], [13], [31], [34]–[36]. Yet, it differs from those suggested for shear-wave anisotropy estimation, which requires either 2-D matrix-array probes [23], [25], [49] or the rotation of linear probes around the axial direction [22], [26], [30], [48]. This difference in setups is a consequence of approximately perpendicular propagation directions of typically excited ultrasound shear and longitudinal waves. In any case, quantifying anisotropy of any kind will require redesigning current ultrasound systems.

The reflector-based setup allows us to measure arrival times of echoes reflected at known distances from the probe. One of the most important results of our work is to show that these traveltimes and anisotropy parameters are nonuniquely related. We demonstrate that anisotropy can be constrained nevertheless by combining measurements from different reflector inclinations. An inclination in the reflector is unavoidable in practice and conventionally regarded as a source of unwanted noise. Here we have resingnified its value and transformed it into a key ingredient for successfully estimating anisotropy. Importantly, we show that two reflector inclinations with relatively small angle differences are sufficient to constrain anisotropy accurately. This facilitates the data acquisition procedure and avoids significant

muscle deformation that could lead to changes in anisotropic properties.

Traveltimes and anisotropy parameters are nonlinearly related; accordingly, we solve the inverse problem using Bayesian inference. Compared to gradient-based optimization techniques, our choice is computationally more demanding and may not suit clinical time constraints. However, it is a powerful approach to quantify uncertainties, crucial for clinical decision-making. In the current implementation, we sample the posterior using the Metropolis-Hastings algorithm, which evaluates approximately 10^5 models per minute on a single CPU from a laptop computer with 15%–20% acceptance rate. This algorithm is known to have a poor acceptance rate, meaning that a large number of samples is needed to approximate the posterior sufficiently well [52]. The performance can be significantly improved by incorporating information from derivatives of the log posterior through Hamiltonian Monte Carlo methods [52], [53]. In this way, we can guide the sampler toward high-probability regions of the model space, making the inversion computationally more attractive.

Since traveltimes are highly sensitive to reflector inclination angles, small angular errors in the forward problem will translate to incorrect anisotropy estimates. We suggest tackling this by considering reflector inclination angles as parameters to invert. Although we could similarly include the probe-reflector distance as another unknown parameter, we consider its uncertainties negligible, following reported values ($5 \mu\text{m}$) in similar works [4]. Under this formulation, our examples show that uncertainties in velocity estimates are sufficiently low to significantly distinguish velocity differences typically observed in muscle tissue ($>10 \text{ m/s}$) [14]–[17]. As suggested by Fig. 10(e), the validity of this conclusion closely depends on the level and nature of observational errors, which in turn depend on the applied traveltime estimation technique. Here we assume normally distributed noise, which may be justified when large measurement errors are minimized by: 1) carefully selecting time intervals of expected first-arrival reflection traveltimes and 2) avoiding outliers due to cycle skips. We can satisfy these conditions with traveltime estimators based on reflector delineation approaches, commonly employed for speed-of-sound tomography [4], [43]. They are designed to remove outliers by including information on the expected reflector depth and forcing smooth traveltime variations between adjacent sensors. However, our study does not consider other sources of errors that may arise in practice (e.g., poor tissue-reflector coupling). Thus, to better understand the clinical potential of our method under realistic conditions, a Bayesian formulation integrating comprehensively and empirically characterized observational errors is required.

For nonlinear problems, the posterior pdf depends on the anisotropy model. Still, we can draw some general conclusions about uncertainties in inferred anisotropy parameters.

- 1) Velocities in directions more parallel to the probe (i.e., fiber direction) are generally less constrained than those in perpendicular directions due to the limited aperture of the acquisition setup.
- 2) The anisotropy angle φ is the least constrained parameter with relative uncertainties that are two orders

of magnitudes larger than those for velocities. In fact, φ becomes increasingly unreliable as velocity differences approach isotropic conditions or the difference between reflector inclination angles becomes very small. Yet, such uncertainties do not affect velocity estimates, which encode more relevant information about tissue anisotropy.

- 3) Overall, the largest standard deviations in φ (3°) are substantially smaller than those reported in similar numerical studies with shear waves (5.6° – 36.3°) [23]. Maximum relative errors in velocities are also considerably lower in our case (0.2% versus 20%) [23]. It suggests that quantifying anisotropy in longitudinal waves could potentially be more robust than in shear waves.

APPENDIX A ELLIPTICAL ANISOTROPY

This appendix discusses the elliptical anisotropy assumption in muscle and shows the conditions under which (1) is satisfied. The wave surface given by (1) is an ellipsoid only if the slowness (reciprocal of the phase velocity) surface is also an ellipsoid [32], [54]. We therefore focus on analyzing the expression for phase velocity.

For simplicity, we consider a transversely isotropic medium with the symmetry axis parallel to x_1 -direction. The elastic stiffness tensor c_{ijkl} characterizing this medium has five independent components, which are $c_{1111} \equiv c_{11}$, $c_{1122} \equiv c_{12}$, $c_{2222} \equiv c_{22}$, $c_{2323} \equiv c_{44}$, and $c_{1212} \equiv c_{66}$ in Voigt notation. The parameters c_{44} and c_{66} are related to shear moduli; thus, in soft tissue, $c_{44}, c_{66} \ll c_{11}, c_{12}, c_{22}$ [29]. We can relate the stiffness tensor to phase velocities V through the Christoffel equation

$$\det[c_{ijkl}n_i n_l - \rho V^2 \delta_{jk}] = 0 \quad (20)$$

where the Einstein summation convention is implied for repeated indices. Here, ρ denotes medium density, the Kronecker delta δ_{jk} is equal to one when $j = k$ and zero otherwise, and n_i refers to the i th component of the wavefront normal vector (slowness vector). By considering a 2-D problem defined in the $x_1 x_2$ plane and taking an arbitrary wavefront direction $\mathbf{n} = (\sin \phi, \cos \phi)$, (20) leads to

$$V^2(\phi) = \frac{1}{2\rho} [c_{11} \sin^2 \phi + c_{22} \cos^2 \phi + G(\phi)] \quad (21)$$

for longitudinal waves, with

$$G(\phi) = \left[(c_{11} \sin^2 \phi - c_{22} \cos^2 \phi)^2 + c_{12}^2 \sin^2 2\phi \right]^{1/2}. \quad (22)$$

The elliptical anisotropy assumption is only valid when the slowness surface in (21) is an ellipse, which is generally not the case. Only when the medium satisfies $c_{12} = (c_{11}c_{22})^{1/2}$, (21) reduces to the ellipse

$$V^2(\phi) = \frac{1}{\rho} [c_{11} \sin^2 \phi + c_{22} \cos^2 \phi] \quad (23)$$

with semiaxes $(\rho/c_{11})^{1/2}$ and $(\rho/c_{22})^{1/2}$. In muscle tissue, empirical studies have shown that $c_{12} \approx (c_{11}c_{22})^{1/2}$ [29], [55], with reported deviations that are below 0.3%. This justifies the elliptical anisotropy model used in this study.

ACKNOWLEDGMENT

The authors gratefully acknowledge the Editor Jeremy Dahl and two anonymous reviewers for the constructive comments that substantially improved the article. They would also like to thank Sergio Sanabria for initial discussions and Christian Boehm for assisting with numerical wave propagation simulations. The Python code used for generating the results of this article can be downloaded from GitHub [56] in the form of self-explanatory Jupyter Notebooks.

REFERENCES

- [1] E. A. O'Flynn *et al.*, "Ultrasound tomography evaluation of breast density: A comparison with noncontrast magnetic resonance imaging," *Investigative Radiol.*, vol. 52, no. 6, pp. 343–348, 2017.
- [2] H. Gemmeke, T. Hopp, M. Zapf, C. Kaiser, and N. V. Rüter, "3D ultrasound computer tomography: Hardware setup, reconstruction methods and first clinical results," *Nucl. Instrum. Methods Phys. Res. A, Accel. Spectrom. Detect. Assoc. Equip.*, vol. 873, pp. 59–65, Nov. 2017.
- [3] M. Jakovljevic, S. Hsieh, R. Ali, G. C. L. Kung, D. Hyun, and J. J. Dahl, "Local speed of sound estimation in tissue using pulse-echo ultrasound: Model-based approach," *J. Acoust. Soc. Amer.*, vol. 144, no. 1, pp. 254–266, 2018.
- [4] S. J. Sanabria, M. B. Rominger, and O. Goksel, "Speed-of-sound imaging based on reflector delineation," *IEEE Trans. Biomed. Eng.*, vol. 66, no. 7, pp. 1949–1962, Jul. 2019.
- [5] J. Wiskin, B. Malik, D. Borup, N. Pirshafiey, and J. Klock, "Full wave 3D inverse scattering transmission ultrasound tomography in the presence of high contrast," *Sci. Rep.*, vol. 10, p. 20166, Nov. 2020.
- [6] N. Korta Martiartu, C. Boehm, and A. Fichtner, "3-D wave-equation-based finite-frequency tomography for ultrasound computed tomography," *IEEE Trans. Ultrason., Ferroelectr., Freq. Control*, vol. 67, no. 7, pp. 1332–1343, Jul. 2020.
- [7] P. Stähli, M. Kuriakose, M. Frenz, and M. Jaeger, "Improved forward model for quantitative pulse-echo speed-of-sound imaging," *Ultrasonics*, vol. 108, Dec. 2020, Art. no. 106168.
- [8] G. Zografos *et al.*, "Novel technology of multimodal ultrasound tomography detects breast lesions," *Eur. Radiol.*, vol. 23, no. 3, pp. 673–683, Mar. 2013.
- [9] L. Ruby *et al.*, "Breast cancer assessment with pulse-echo speed of sound ultrasound from intrinsic tissue reflections: Proof-of-concept," *Investigative Radiol.*, vol. 54, no. 7, pp. 419–427, 2019.
- [10] M. Dioguardi Burgio *et al.*, "Ultrasonic adaptive sound speed estimation for the diagnosis and quantification of hepatic steatosis: A pilot study," *Ultraschall der Medizin-Eur. J. Ultrasound*, vol. 40, no. 6, pp. 722–733, 2019.
- [11] M. Imbault *et al.*, "Robust sound speed estimation for ultrasound-based hepatic steatosis assessment," *Phys. Med. Biol.*, vol. 62, no. 9, pp. 3582–3598, Apr. 2017.
- [12] S. J. Sanabria *et al.*, "Speed of sound ultrasound: A pilot study on a novel technique to identify sarcopenia in seniors," *Eur. Radiol.*, vol. 29, no. 1, pp. 3–12, Jan. 2019.
- [13] L. Ruby *et al.*, "Speed of sound ultrasound: Comparison with proton density fat fraction assessed with Dixon MRI for fat content quantification of the lower extremity," *Eur. Radiol.*, vol. 30, no. 10, p. 5272, 2020.
- [14] C. R. Mol and P. A. Breddels, "Ultrasound velocity in muscle," *J. Acoust. Soc. Amer.*, vol. 71, no. 2, pp. 455–461, 1982.
- [15] D. E. Goldman and J. R. Richards, "Measurement of high-frequency sound velocity in mammalian soft tissues," *J. Acoust. Soc. Amer.*, vol. 26, no. 6, pp. 981–983, 1954.
- [16] W. D. O'Brien and J. E. Olerud, "Ultrasonic assessment of tissue anisotropy," in *Proc. IEEE Ultrason. Symp. Int. Symp.*, vol. 2, Nov. 1995, pp. 1145–1148.
- [17] E. D. Verdonk, S. A. Wickline, and J. G. Miller, "Anisotropy of ultrasonic velocity and elastic properties in normal human myocardium," *J. Acoust. Soc. Amer.*, vol. 92, no. 6, pp. 3039–3050, Dec. 1992.
- [18] K. A. Topp and W. D. O'Brien, "Anisotropy of ultrasonic propagation and scattering properties in fresh rat skeletal muscle *in vitro*," *J. Acoust. Soc. Amer.*, vol. 107, no. 2, pp. 1027–1033, 2000.
- [19] B. H. Goodpaster *et al.*, "The loss of skeletal muscle strength, mass, and quality in older adults: The health, aging and body composition study," *J. Gerontol. A, Biol. Sci. Med. Sci.*, vol. 61, no. 10, pp. 1059–1064, Oct. 2006.
- [20] A. J. Cruz-Jentoft *et al.*, "Sarcopenia: Revised European consensus on definition and diagnosis," *Age Ageing*, vol. 48, no. 1, pp. 16–31, Jan. 2019.
- [21] M. V. Narici, C. N. Maganaris, N. D. Reeves, and P. Capodaglio, "Effect of aging on human muscle architecture," *J. Appl. Physiol.*, vol. 95, no. 6, pp. 2229–2234, Dec. 2003.
- [22] W. Lee *et al.*, "Mapping myocardial fiber orientation using echocardiography-based shear wave imaging," *IEEE Trans. Med. Imag.*, vol. 31, no. 3, pp. 554–562, Mar. 2012.
- [23] M. Correia, T. Deffieux, S. Chatelin, J. Provost, M. Tanter, and M. Pernot, "3D elastic tensor imaging in weakly transversely isotropic soft tissues," *Phys. Med. Biol.*, vol. 63, no. 15, Jul. 2018, Art. no. 155005.
- [24] W.-N. Lee, B. Larrat, M. Pernot, and M. Tanter, "Ultrasound elastic tensor imaging: Comparison with MR diffusion tensor imaging in the myocardium," *Phys. Med. Biol.*, vol. 57, no. 16, pp. 5075–5095, Jul. 2012.
- [25] M. Wang, B. Byram, M. Palmeri, N. Rouze, and K. Nightingale, "Imaging transverse isotropic properties of muscle by monitoring acoustic radiation force induced shear waves using a 2-D matrix ultrasound array," *IEEE Trans. Med. Imag.*, vol. 32, no. 9, pp. 1671–1684, Sep. 2013.
- [26] M. M. Hossain, C. J. Moore, and C. M. Gallippi, "Acoustic radiation force impulse-induced peak displacements reflect degree of anisotropy in transversely isotropic elastic materials," *IEEE Trans. Ultrason., Ferroelectr., Freq. Control*, vol. 64, no. 6, pp. 989–1001, Jun. 2017.
- [27] M. M. Hossain *et al.*, "Mechanical anisotropy assessment in kidney cortex using ARFI peak displacement: Preclinical validation and pilot *in vivo* clinical results in kidney allografts," *IEEE Trans. Ultrason., Ferroelectr., Freq. Control*, vol. 66, no. 3, pp. 551–562, Mar. 2019.
- [28] T. Glozman and H. Azhari, "A method for characterization of tissue elastic properties combining ultrasonic computed tomography with elastography," *J. Ultrasound Med.*, vol. 29, no. 3, pp. 387–398, Mar. 2010.
- [29] S. F. Levinson, "Ultrasound propagation in anisotropic soft tissues: The application of linear elastic theory," *J. Biomech.*, vol. 20, no. 3, pp. 251–260, Jan. 1987.
- [30] J.-L. Gennisson, T. Deffieux, E. Macé, G. Montaldo, M. Fink, and M. Tanter, "Viscoelastic and anisotropic mechanical properties of *in vivo* muscle tissue assessed by supersonic shear imaging," *Ultrasound Med. Biol.*, vol. 36, no. 5, pp. 789–801, 2010.
- [31] N. Korta Martiartu, D. Nakhostin, L. Ruby, T. Frauenfelder, M. B. Rominger, and S. J. Sanabria, "Speed of sound and shear wave speed for calf soft tissue composition and nonlinearity assessment," *Quant. Imag. Med. Surg.*, vol. 11, no. 9, pp. 4149–4161, Sep. 2021.
- [32] B. S. Byun, "Seismic parameters for media with elliptical velocity dependencies," *Geophysics*, vol. 47, no. 12, pp. 1621–1626, Dec. 1982.
- [33] N. Korta Martiartu *et al.*, "Speed-of-sound anisotropy estimation using reflector-based pulse-echo ultrasound," in *Medical Imaging: Ultrasonic Imaging and Tomography* (International Society for Optics and Photonics), vol. 11602, B. C. Byram and N. V. Rüter, Eds. Bellingham, WA, USA: SPIE, 2021.
- [34] S. J. Sanabria *et al.*, "Breast-density assessment with hand-held ultrasound: A novel biomarker to assess breast cancer risk and to tailor screening?" *Eur. Radiol.*, vol. 28, no. 8, pp. 3165–3175, 2018.
- [35] L. Ruby *et al.*, "Breast density assessment in young women with ultrasound based on speed of sound: Influence of the menstrual cycle," *Medicine*, vol. 98, no. 25, 2019, Art. no. e16123.
- [36] L. Ruby *et al.*, "Quantification of immobilization-induced changes in human calf muscle using speed-of-sound ultrasound: An observational pilot study," *Medicine*, vol. 100, no. 10, 2021, Art. no. e23576.
- [37] S. J. Sanabria and O. Goksel, "Hand-held sound-speed imaging based on ultrasound reflector delineation," in *Medical Image Computing and Computer-Assisted Intervention—(MICCAI)*, S. Ourselin, L. Joskowicz, M. R. Sabuncu, G. Unal, and W. Wells, Eds. Cham, Switzerland: Springer, 2016, pp. 568–576.

- [38] M. Afanasiev *et al.*, “Modular and flexible spectral-element waveform modelling in two and three dimensions,” *Geophys. J. Int.*, vol. 216, no. 3, pp. 1675–1692, Mar. 2019.
- [39] A. Tarantola, *Inverse Problem Theory and Methods for Model Parameter Estimation*. Philadelphia, PA, USA: SIAM, 2005.
- [40] K. Mosegaard and A. Tarantola, “Monte Carlo sampling of solutions to inverse problems,” *J. Geophys. Res., Solid Earth*, vol. 100, no. B7, pp. 12431–12447, Jul. 1995.
- [41] T. Bayes and R. Price, “An essay towards solving a problem in the doctrine of chances,” *Philos. Trans. Roy. Soc. London*, vol. 53, pp. 370–418, 1763.
- [42] A. Tarantola and B. Valetier, “Inverse problems= quest for information,” *J. Geophys.*, vol. 50, no. 1, pp. 159–170, 1982.
- [43] B. R. Chintada, R. Rau, and O. Goksel, “Time of arrival delineation in echo traces for reflection ultrasound tomography,” in *Proc. IEEE 18th Int. Symp. Biomed. Imag. (ISBI)*, Apr. 2021, pp. 1342–1345.
- [44] N. Korta Martiartu, C. Boehm, V. Hapla, H. Maurer, I. J. Balic, and A. Fichtner, “Optimal experimental design for joint reflection-transmission ultrasound breast imaging: From ray- to wave-based methods,” *J. Acoust. Soc. Amer.*, vol. 146, no. 2, pp. 1252–1264, Aug. 2019.
- [45] N. Metropolis, A. W. Rosenbluth, M. N. Rosenbluth, A. H. Teller, and E. Teller, “Equation of state calculations by fast computing machines,” *J. Chem. Phys.* vol. 21, no. 6, pp. 1087–1092, 1953.
- [46] W. K. Hastings, “Monte Carlo sampling methods using Markov chains and their applications,” *Biometrika*, vol. 57, no. 1, pp. 97–109, Apr. 1970.
- [47] L. Tierney, “Markov chains for exploring posterior distributions,” *Ann. Statist.*, vol. 22, no. 4, pp. 1701–1728, Dec. 1994.
- [48] J.-L. Gennisson, S. Catheline, S. Chaffai, and M. Fink, “Transient elastography in anisotropic medium: Application to the measurement of slow and fast shear wave speeds in muscles,” *J. Acoust. Soc. Amer.*, vol. 114, no. 1, pp. 536–541, 2003.
- [49] M. M. Hossain and C. M. Gallippi, “Electronic point spread function rotation using a three-row transducer for ARFI-based elastic anisotropy assessment: In silico and experimental demonstration,” *IEEE Trans. Ultrason., Ferroelectr., Freq. Control*, vol. 68, no. 3, pp. 632–646, Mar. 2021.
- [50] G. E. Backus, “Long-wave elastic anisotropy produced by horizontal layering,” *J. Geophys. Res.*, vol. 67, no. 11, pp. 4427–4440, 1962.
- [51] T. H. Jordan, “An effective medium theory for three-dimensional elastic heterogeneities,” *Geophys. J. Int.*, vol. 203, no. 2, pp. 1343–1354, Nov. 2015.
- [52] M. Betancourt, “A conceptual introduction to Hamiltonian Monte Carlo,” 2018, *arXiv:1701.02434*.
- [53] S. Duane, A. D. Kennedy, B. J. Pendleton, and D. Roweth, “Hybrid Monte Carlo,” *Phys. Lett. B*, vol. 195, no. 2, pp. 216–222, Sep. 1987.
- [54] K. Helbig, “Elliptical anisotropy—Its significance and meaning,” *Geophysics*, vol. 48, no. 7, pp. 825–832, 1983.
- [55] D. Royer, J. L. Gennisson, T. Deffieux, and M. Tanter, “On the elasticity of transverse isotropic soft tissues (L),” *J. Acoust. Soc. Amer.*, vol. 129, pp. 2757–2760, May 2011.
- [56] N. Korta Martiartu. (Feb. 2022). *MCMC SoS Anisotropy Estimation With Pulse-Echo Ultrasound*. [Online]. Available: <https://github.com/naiarako/UltrasoundAnisotropy>